Supporting Online Material for

Gravity Field and Internal Structure of Mercury from MESSENGER

David E. Smith, Maria T. Zuber,* Roger J. Phillips, Sean C. Solomon,
Steven A. Hauck II, Frank G. Lemoine, Erwan Mazarico, Gregory A. Neumann,
Stanton J. Peale, Jean-Luc Margot, Catherine L. Johnson, Mark H. Torrence,
Mark E. Perry, David D. Rowlands, Sander Goossens,
James W. Head, Anthony H. Taylor

*To whom correspondence should be addressed. E-mail: zuber@mit.edu

Published 21 March 2012 on *Science* Express
DOI: 10.1126/science.1218809

This PDF file includes:

Supplementary Materials

Method of Solution

The HgM002 20 × 20 harmonic solution for Mercury's gravity field used 129 daily orbital arcs, shown in Fig. S1, derived from X-band Doppler tracking of the MESSENGER spacecraft during the period 18 March to 23 August 2011. The solution also included X-band Doppler data from the first two MESSENGER flybys (designated M1 and M2) of Mercury (*6*). A total of 1.2 million observations contributed to this solution.

Processing of Deep Space Network (DSN) data from MESSENGER was accomplished using the NASA Goddard Space Flight Center (GSFC) Orbit Determination and Geodetic Parameter Estimation Program (GEODYN) (*30*). The planetary orientation model (*31*) incorporated values of Mercury's physical and rotational parameters including the longitudinal librations. When the data were processed in daily (24-h) arcs, the typical fit to the Doppler data had residuals of ~0.4 ± 0.2 mm s^{-1}, several times the noise level of the DSN data (~0.1 mm s^{-1}). We excluded tracking observations closest to superior conjunction in these solutions. Once normal equations were obtained by the GEODYN program, solutions for Mercury's gravity field were obtained via NASA GSFC SOLVE software (*32*) in a fashion similar to those used for gravity field solutions for the Moon (*33*) and Mars (*34*).

In constructing solutions for the gravitational field, the orbit and data modeling accounted for solar radiation pressure, planetary radiation pressure induced by the reflected solar and thermal radiation from the planet Mercury, third-body gravity perturbations from the Sun and other planets, and relativistic corrections including the modification of the central body term in the force model and light-time effects in the measurement model. A mean planetary albedo of 0.074 and a recent planetary thermal model (*35*) were used. The tracking data were corrected for DSN station coordinate effects, including Earth's polar motion, solid-Earth tides, and ocean loading. Meteorological data at the stations were used to correct the radiometric tracking data for propagation effects through Earth's troposphere.

The modeling included a box-wing representation of the MESSENGER probe that approximates the spacecraft as a series of flat plates with specific cross-sectional areas and specular and diffuse reflectivities. The plates were oriented in space by means of the spacecraft attitude data (quaternions) (*36*).

MESSENGER does not have a steerable high-gain antenna (as, for example, on the Mars Reconnaissance Orbiter) but relies on six separate antennae mounted on different faces of the spacecraft, each with a distinct offset with respect to the center of mass of the spacecraft. The processing of the tracking data accounted for the routine switching among the different antennae, for which the schedule of use for tracking varies by day and mission phase. Each of the offsets of the MESSENGER tracking antennae from the spacecraft center of mass was explicitly modeled.

A spherical harmonic solution for the gravity field was produced from the assembled orbital arcs using the NASA/GSFC SOLVE program (*32*). The gravitational potential, *U*, is represented as a spherical harmonic expansion with normalized coefficients ($\bar{C}_{nm}$, $\bar{S}_{nm}$), expressed after (*29*) as

$$U = \frac{GM}{r} + \frac{GM}{r}\sum_{n=2}^{\infty}\sum_{m=0}^{n}\left(\frac{R_M}{r}\right)^n \bar{P}_{nm}(\sin\varphi)\left[\bar{C}_{nm}\cos(m\lambda) + \bar{S}_{nm}\sin(m\lambda)\right], \quad (1)$$

where GM is the gravitational constant times Mercury's mass, n and m are the spherical harmonic degree and order, $\bar{P}_{nm}$ are normalized associated Legendre polynomials, R_M is Mercury's reference radius (*3*), ϕ is latitude, and λ is longitude. The normalized and unnormalized gravitational coefficients are related by (*29*)

$$\begin{pmatrix} C_{nm} \\ S_{nm} \end{pmatrix} = \left[\frac{(n-m)!(2n+1)(2-\delta_{0m})}{(n+m)!}\right]^{1/2}\begin{pmatrix} \bar{C}_{nm} \\ \bar{S}_{nm} \end{pmatrix} = f_{nm}\begin{pmatrix} \bar{C}_{nm} \\ \bar{S}_{nm} \end{pmatrix}. \quad (2)$$

Given the temporal span of the data and Mercury's low spin rate, we did not solve for the solid-planet tidal Love number but rather used a fixed value ($k_2 = 0.2$). The solid-planet tide can alias into our recovery of the gravitational flattening, C_{20}, but that contribution is expected to be very small (~0.001 C_{20}), which we confirmed by obtaining an alternative solution with a different *a priori* value of k_2 (= 0.6).

The MESSENGER navigation team conducted an independent analysis and produced an independent solution for Mercury's gravity field using MESSENGER orbital tracking data through 5 October 2011. The Doppler observations were processed using the Jet Propulsion Laboratory MIRAGE software, and the solution agrees closely with HgM002 with respect to the values of the degree-2 terms and the pattern of gravity anomalies in the northern hemisphere.

Analysis of the Gravitational Field

The power in the gravitational field, expressed as root mean squared (RMS) power, is given in Fig. S2. To limit the power of the high-degree coefficients because of noise in areas that lack low-altitude coverage, a Kaula power-law constraint (*29*) was applied to coefficients for spherical harmonic degrees greater than $l = 2$. That constraint ($4 \times 10^{-5}/l^2$) was derived from scaling of gravitational power for the Moon (cf. Fig. S2). Gravity anomaly errors are given in Fig. S3, which shows that projected errors derived from the covariance of the 20×20 solution are below 20 mGal north of 30°N. Correlations between low-degree coefficients are shown in Fig. S4. The correlation matrix indicates that zonal coefficients exhibit higher intra-order correlations than tesseral or sectoral coefficients, with the highest correlation between C_{20} and C_{30}. The first two MESSENGER flybys of Mercury were valuable in constraining GM, the product of the gravitational constant G and Mercury's mass M, and reducing its correlation with C_{20}.

To better understand the error characteristics of the low-degree field, the HgM002 covariance matrix was used to generate clone models and to analyze the distribution of spherical harmonic coefficients. To generate a clone gravity model, the covariance matrix was diagonalized. Subsequently, each eigenvector was multiplied by ±1 times the square root of its eigenvalue in a random fashion, and the difference coefficients of the field were generated. More than 50000 clone models were evaluated (cf. Fig. S5).

Relations between perturbed and non-perturbed values of the C_{20} and C_{22} coefficients are plotted in Fig. S6. We processed the MESSENGER Doppler data from 19 March to 5 June 2011 simultaneously with approximately 2700 altimeter crossovers derived from MESSENGER's Mercury Laser Altimeter (MLA) (*3*). The RMS fit to the altimeter

crossovers (which were not included in the orbit solution) with HgM002 is about 80 m. Fig. S6 shows that if the C_{20} and C_{22} values are perturbed by ±10 percent, the altimeter crossover RMS fit degrades to 180–230 m. This test provides a strong validation of the values for C_{20} and C_{22} obtained with the HgM002 solution.

Gravity Modeling

We generated model gravity predictions to compare with the HgM002 solution by calculating the "degree of compensation" (*37*), a calculation that employs a spherical harmonic formalism to describe the flexural and membrane response to a surface load (e.g., shape) for which some level of compensation takes place at the crust-mantle boundary. The degree of compensation was folded into the isostatic response function, which maps shapes of the surface and crust-mantle boundaries into the model gravity predications. Parameters in the model are the Young's modulus (100 GPa) and Poisson's ratio (0.25) of the elastic lithosphere, crustal density (3100 kg m^{-3}), mantle density (3300 kg m^{-3}), reference crustal thickness (h_c, variable), and thickness of the elastic lithosphere (T_e, variable). The h_c-T_e parameter space was searched for model gravity solutions that best fit the HgM002 gravity solution in the vicinity of Mercury's northern rise. Best-fitting solutions (Fig. S7) had fit standard deviations of 7 mGal (cf. the peak gravity anomaly for the northern rise is ~150 mGal), and the variance of the northern-rise gravity anomaly was reduced 99.7% by the models. The 70-90 km range found for T_e will lead to a small curvature of the load-induced deflection, so the thickness of the mechanical lithosphere (the outermost shell of the planet displaying long-term strength) will be approximately that of the elastic lithosphere.

References

1. S. C. Solomon, R. L. McNutt, Jr., R. E. Gold, D. L. Domingue, MESSENGER mission overview. *Space Sci. Rev.* **131**, 3 (2007). doi:10.1007/s11214-007-9247-6
2. Materials and methods are available as supplementary materials on *Science* Online.
3. M. T. Zuber *et al.*, Topography of the northern hemisphere of Mercury from MESSENGER laser altimetry. *Science* **336** (2012); published online 21 March 2012; 10.1126/science.1218805.
4. P. M. Muller, W. L. Sjogren, Mascons: Lunar mass concentrations. *Science* **161**, 680 (1968).doi:10.1126/science.161.3842.680 Medline
5. D. E. Smith *et al*., An improved gravity model for Mars: Goddard Mars Model-1 (GMM-1). *J. Geophys. Res.* **98**, (E11), 20871 (1993).doi:10.1029/93JE01839
6. D. E. Smith *et al*., The equatorial shape and gravity field of Mercury from MESSENGER flybys 1 and 2. *Icarus* **209**, 88 (2010). doi:10.1016/j.icarus.2010.04.007
7. J. D. Anderson, J. Palguta, G. Schubert, Constraining the location and dimensions of mass anomalies on Mercury from Mariner 10 Doppler data. Abstract P41A-1572, paper presented at the American Geophysical Union Fall Meeting, San Francisco, Calif., 5-9 Dec. (2011).
8. L. R. Nittler *et al*., The major-element composition of Mercury's surface from MESSENGER x-ray spectrometry. *Science* **333**, 1847 (2011).doi:10.1126/science.1211567 Medline
9. L. R. Nittler *et al*., Major elements on Mercury's surface from MESSENGER x-ray spectrometry. Abstract 142-3, paper presented at the Geological Society of America Annual Meeting, Minneapolis, Minn., 9-12 October (2011).
10. B. Charlier, T. L. Grove, M. T. Zuber, Composition and differentiation of 'basalts' at the surface of Mercury. *Lunar Planet. Sci.* **43**, abstract 1400 (2012).
11. M. T. Zuber *et al*., Laser altimeter observations from MESSENGER's first Mercury flyby. *Science* **321**, 77 (2008).doi:10.1126/science.1159086 Medline
12. F. Nimmo, T. R. Watters, Depth of faulting on Mercury: Implications for heat flux and crustal and effective elastic thickness. *Geophys. Res. Lett.* **31**, L02701 (2004). doi:10.1029/2003GL018847
13. G. A. Neumann, M. T. Zuber, D. E. Smith, F. G. Lemoine, The lunar crust: Global structure and signature of major basins. *J. Geophys. Res.* **101**, (E7), 16841 (1996). doi:10.1029/96JE01246
14. M. T. Zuber *et al*., Internal structure and early thermal evolution of Mars from Mars Global Surveyor topography and gravity. *Science* **287**, 1788 (2000).doi:10.1126/science.287.5459.1788 Medline
15. J. W. Head *et al*., Flood volcanism in the northern high latitudes of Mercury revealed by MESSENGER. *Science* **333**, 1853 (2011).doi:10.1126/science.1211997 Medline
16. R. G. Strom, G. A. Neumann, in *Mercury*, F. Villas, C. R. Chapman, M. S. Matthews, Eds. (Univ. Arizona Press, Tucson, 1988), pp. 363–373.
17. P. J. McGovern *et al*., Correction to "Localized gravity/topography admittances and correlation spectra on Mars: Implications for regional and global evolution". *J. Geophys. Res.* **109**, (E7), E07007 (2004). doi:10.1029/2004JE002286
18. J.-L. Margot, S. J. Peale, R. F. Jurgens, M. A. Slade, I. V. Holin, Large longitude libration of Mercury reveals a molten core. *Science* **316**, 710 (2007).doi:10.1126/science.1140514 Medline

19. S. J. Peale, Does Mercury have a molten core? *Nature* **262**, 765 (1976). doi:10.1038/262765a0
20. S. J. Peale, R. J. Phillips, S. C. Solomon, D. E. Smith, M. T. Zuber, A procedure for determining the nature of Mercury's core. *Meteorit. Planet. Sci.* **37**, 1269 (2002). doi:10.1111/j.1945-5100.2002.tb00895.x
21. M. Yseboodt, J.-L. Margot, Evolution of Mercury's obliquity. *Icarus* **181**, 327 (2006). doi:10.1016/j.icarus.2005.11.024
22. J.-L. Margot, S. Padovan, S. J. Peale, S. C. Solomon, Measurements of Mercury's spin state and inferences about its interior. Abstract P41A-1573, paper presented at the American Geophysical Union Fall Meeting, San Francisco, Calif., 5–9 Dec. (2011).
23. S. A. Hauck, II, S. C. Solomon, D. A. Smith, Predicted recovery of Mercury's internal structure by MESSENGER. *Geophys. Res. Lett.* **34**, L18201 (2007). doi:10.1029/2007GL030793
24. V. Malavergne, M. J. Toplis, S. Berthet, J. Jones, Highly reducing conditions during core formation on Mercury: Implications for internal structure and the origin of a magnetic field. *Icarus* **206**, 199 (2010). doi:10.1016/j.icarus.2009.09.001
25. G. Morard, T. Katsura, Pressure-temperature cartography of Fe-S-Si immiscible system. *Geochim. Cosmochim. Acta* **74**, 3659 (2010). doi:10.1016/j.gca.2010.03.025
26. U. R. Christensen, A deep dynamo generating Mercury's magnetic field. *Nature* **444**, 1056 (2006).doi:10.1038/nature05342 Medline
27. S. A. Hauck, II, A. J. Dombard, R. J. Phillips, S. C. Solomon, Internal and tectonic evolution of Mercury. *Earth Planet. Sci. Lett.* **222**, 713 (2004). doi:10.1016/j.epsl.2004.03.037
28. M. T. Zuber *et al*., Accommodation of lithospheric shortening on Mercury from altimetric profiles of ridges and lobate scarps measured during MESSENGER flybys 1 and 2. *Icarus* **209**, 88 (2010). doi:10.1016/j.icarus.2010.02.026
29. W. M. Kaula, *Theory of Satellite Geodesy* (Blaisdell, Waltham, 1966).
30. D. E. Pavlis, S. G. Poulose, J. J. McCarthy, GEODYN Operations Manuals (SGT, Inc., Greenbelt, Md., 2009).
31. J.-L. Margot, A Mercury orientation model including non-zero obliquity and libration. *Celestial Mech. Dyn. Astron.* **105**, 329 (2009). doi:10.1007/s10569-009-9234-1
32. R. E. Ulman, "SOLVE Program: Mathematical Formulation and Guide to User Input" (Hughes/STX Contractor Report, contract NAS5-31760, 1994).
33. E. Mazarico, F. G. Lemoine, S.-C. Han, D. E. Smith, GLGM-3, a degree-150 lunar gravity model from the historical tracking data of NASA Moon orbiters. *J. Geophys. Res.* **115**, (E5), E05001 (2010). doi:10.1029/2009JE003472
34. F. G. Lemoine *et al*., An improved solution of the gravity field of Mars (GMM-2B) from Mars Global Surveyor. *J. Geophys. Res.* **106**, (E10), 23,359 (2001). doi:10.1029/2000JE001426
35. D. P. Paige *et al*., Thermal stability of frozen volatiles in the north polar region of Mercury, *Lunar Planet. Sci. Conf.* **43,** #2875 (2012).
36. J. A. Marshall, S. B. Luthcke, Modeling radiation forces acting on TOPEX/Poseidon for precision orbit determination. *J. Spacecr. Rockets* **31**, 99 (1994). doi:10.2514/3.26408
37. D. L. Turcotte, R. J. Willemann, W. F. Haxby, J. Norberry, Role of membrane stresses in the support of planetary topography. *J. Geophys. Res.* **86**, (B5), 3951 (1981). doi:10.1029/JB086iB05p03951

FIGURES

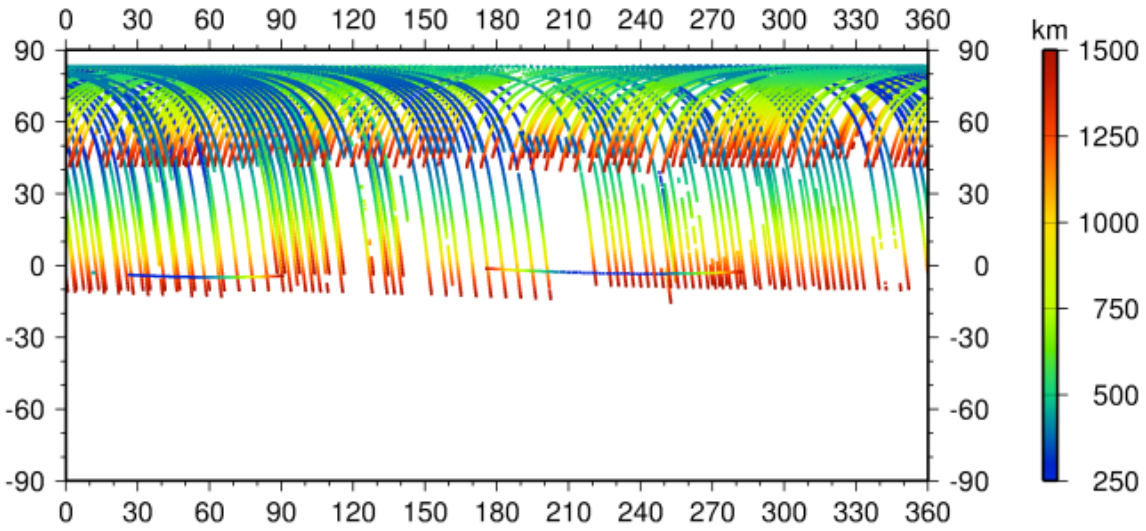

Figure S1. Distribution of Doppler tracking data acquired when the MESSENGER spacecraft was within 1500-km altitude of the surface of Mercury (cylindrical projection). Color coding indicates spacecraft altitude.

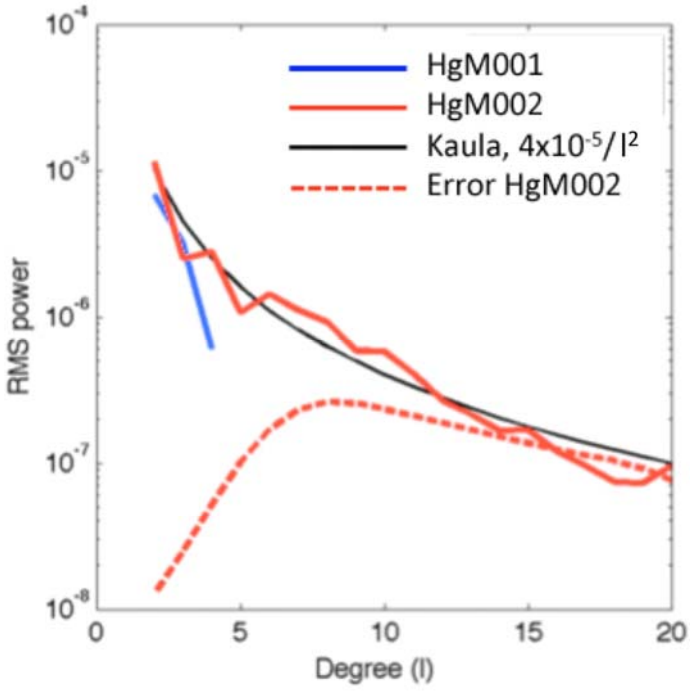

Figure S2. RMS power for solution HgM002. Variances for earlier solution HgM001 (*6*) are also shown, as are the adopted Kaula constraint (*29*) and the errors in solution HgM002 by harmonic degree.

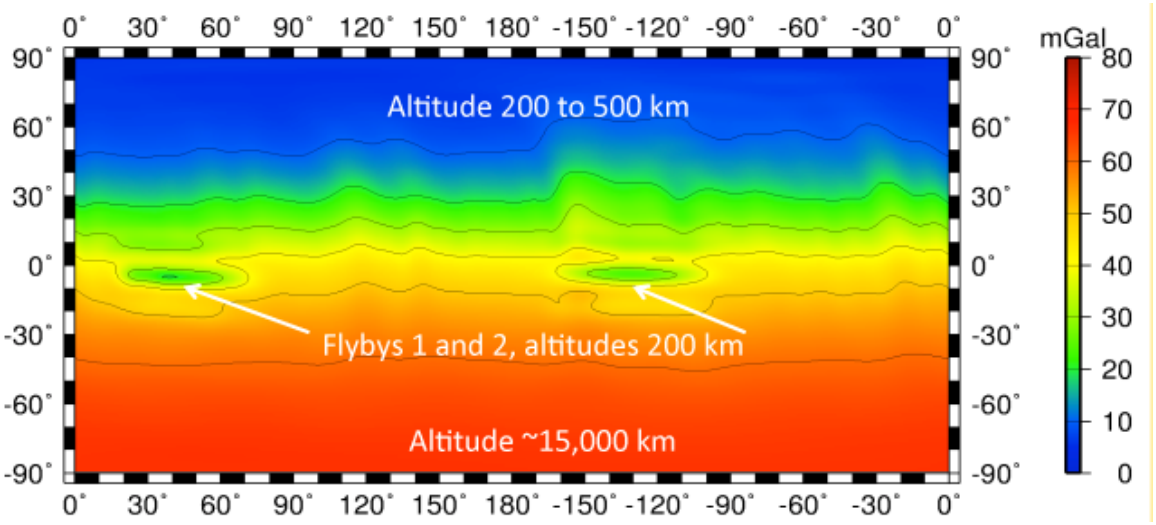

Figure S3. Cylindrical projection of gravity anomaly errors for solution HgM002.

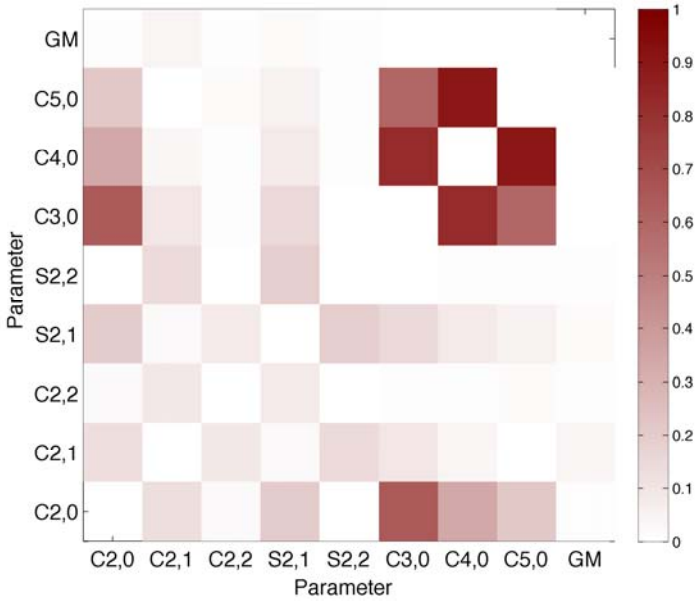

Figure S4. Correlation matrix for *GM* and the low-degree harmonic coefficients in the HgM002 solution.

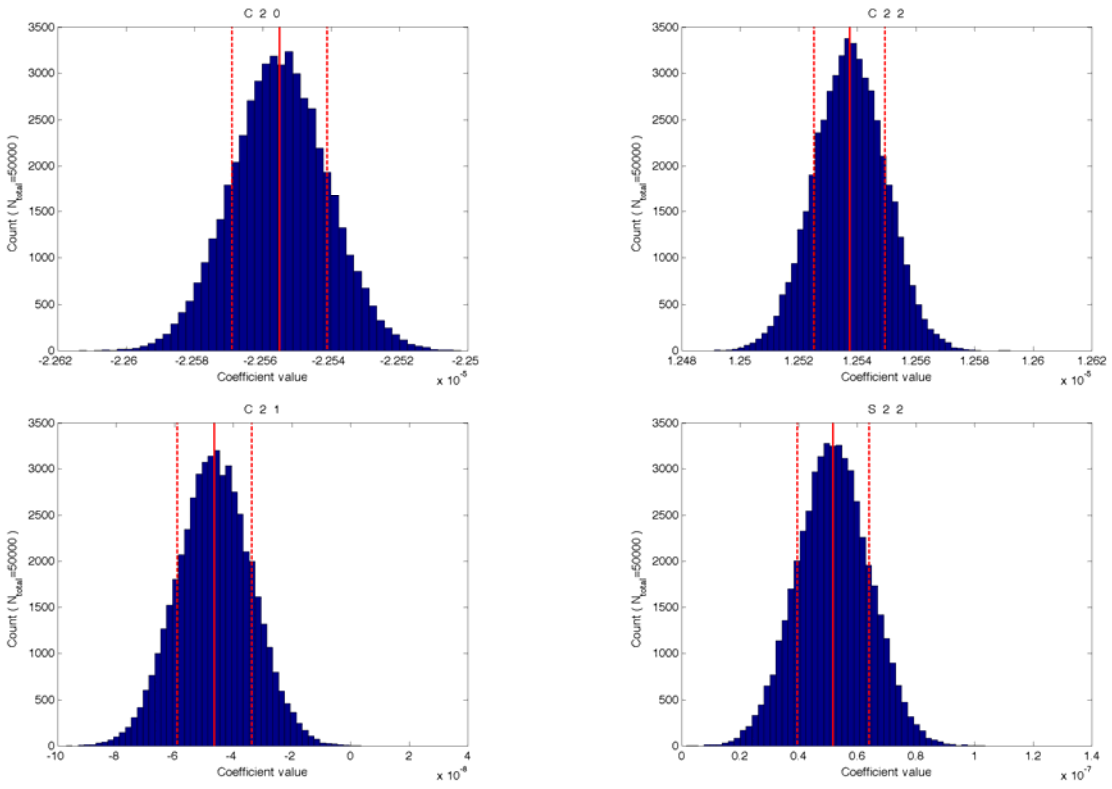

Figure S5. Distribution of selected coefficient values from the analysis of clone models.

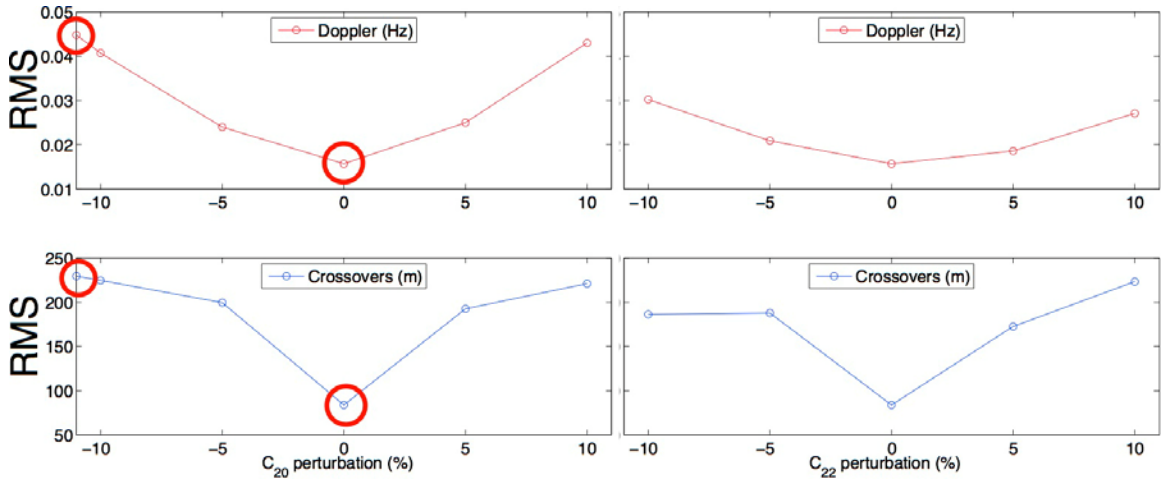

Figure S6. Validation of recovery of C_{20} (left) and C_{22} (right) from Doppler (top) and altimeter crossover (bottom) data in an arc using data between 9 March and 5 June 2011. The best-fit value for each coefficient, with corresponding minimum RMS residual, represents the zero-percent perturbation point along each abscissa. Perturbing the solution in either direction increases the RMS residual. The Doppler X-band residuals are expressed in Hz, and the altimeter crossover residuals are expressed in m.

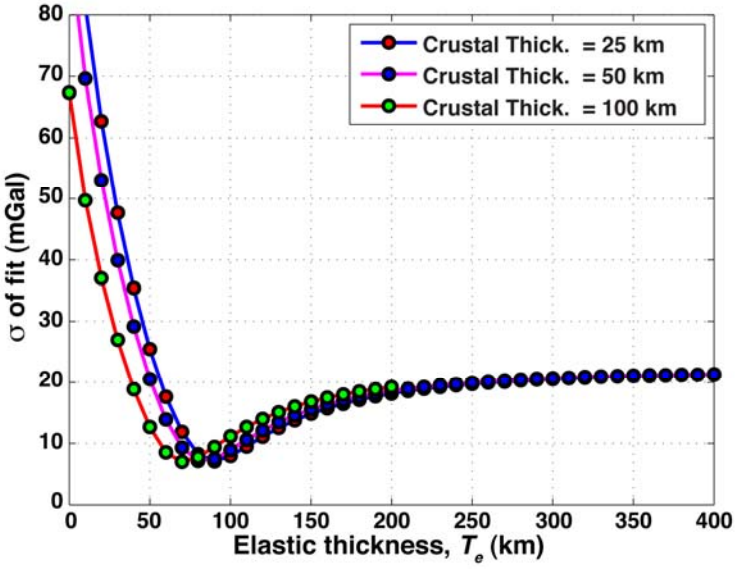

Figure S7. Standard deviation (σ) of the residuals from fits of the model gravity to HgM002 gravity in the vicinity of Mercury's northern rise. Results are shown for three different values of crustal thickness (h_c). The best fitting elastic lithosphere thicknesses are relatively insensitive to crustal thickness values.